



Cite this: *J. Mater. Chem. B*, 2025, 13, 524

Synergistic microwave hyperthermia treatment for subcutaneous deep *in situ* breast cancer using conformal array antennas and a microwave-thermal-sensitive nanomaterial†

Xinyu Zhang,^{ab} Yongxing Du,^{*b} Ling Qin,^b Baoshan Li,^b Qiong Wu^a and Xianwei Meng^{id} ^{*a}

When microwave hyperthermia (MWH) array antenna technology is used to treat breast cancer, how to effectively target and heat deep tumors and reduce thermal damage to healthy tissues is still a challenge in clinical applications. In this study, the synergistic MWH effect of conformal-array antennas (CAA) and a novel microwave-thermal-sensitive nanomaterial (MTSN) was investigated for the treatment of subcutaneous deep *in situ* breast cancer. At the beginning of the study, the thermal damage score was used to evaluate the therapeutic efficacy of the CAA. It was found that although array antenna technology can achieve effective heating of deep tumors, its damage to healthy tissues is unacceptable. Consequently, we developed a novel MTSN, ZIF-8@HA, whose unique structure significantly enhanced the absorption of MW energy and MW thermal conversion efficiency in the local tumor region. The MW thermal conversion efficiency of ZIF-8@HA achieved was as high as 46.46% in *in vivo* MW heating experiments. In the phantom that simulates the electromagnetic environment of the human body, the microwave-thermal sensitization (MTS) effect is also significant, and the reduction in the average thermal damage score of healthy tissues by more than 10% was verified through measurements using the coaxial probe method and COMSOL simulations. Cellular experiments confirmed that the combination of ZIF-8@HA and MW irradiation could significantly reduce the survival rate of tumor cells. In addition, cross-tissue MW heating experiments revealed the advantages of ZIF-8@HA combined with the CAA. Finally, phantom experiments confirmed that the synergistic use of the CAA with ZIF-8@HA significantly accelerated the local heating rate of deep tumors, reduced the time required for the tumor region to achieve 100% thermal damage, and effectively minimized the thermal damage to healthy tissues.

Received 15th October 2024,
Accepted 15th November 2024

DOI: 10.1039/d4tb02319f

rsc.li/materials-b

1. Introduction

Breast cancer is a major threat to global women's health, with persistently high incidence rates, ranking first among malignant tumors in women.¹ In the treatment of breast cancer with microwave hyperthermia (MWH), array antenna technology has demonstrated unique advantages due to its ability to precisely target tumor tissues while minimizing the impact on surrounding healthy tissues.^{2–4} Nonetheless, this technology still faces challenges in clinical applications, particularly in how to

effectively heat deep-seated tumors and reduce thermal damage to surrounding healthy tissues.⁵ The crux of these issues lies in improving the transmission efficiency of microwave (MW) energy in biological tissues and accurately controlling the thermal dose. Therefore, the development of new technologies to optimize the effects of MWH has become an urgent task in the field of breast cancer treatment.

Array antenna technology, as a key innovation in MWH, has been proven to effectively enhance the heating capability of deep-seated tumors.^{2,6,7} This technology achieves precise heating of the tumor region by coherently superimposing the electric fields of individual array elements onto the tumor target area.^{8–10} However, despite advancements in targeted heating capabilities, this technology still faces the risk of causing undesired thermal damage to healthy tissues during deep tumor treatment. Although existing studies have considered that continuous heating at a certain power level for a period can achieve the target temperature, effective strategies

^a Laboratory of Controllable Preparation and Application of Nanomaterials, Technical Institute of Physics and Chemistry, Chinese Academy of Sciences, No. 29 East Road Zhongguancun, Beijing 100190, P. R. China.

E-mail: mengxw@mail.ipc.ac.cn

^b School of Digital and Intelligence Industry, Inner Mongolia University of Science and Technology, Baotou 014010, China. E-mail: dyxql@imust.edu.cn

† Electronic supplementary information (ESI) available. See DOI: <https://doi.org/10.1039/d4tb02319f>



are still lacking for ensuring complete ablation of tumor tissue while protecting surrounding healthy tissue.^{4,6,11,12} Despite previous studies attempting to reduce thermal damage to surrounding tissues by adjusting the specific absorption rate (SAR) distribution,^{13,14} these methods often come at the expense of the thermal dose to the tumor tissue, failing to achieve an optimized therapeutic balance.

In MWH, the use of microwave-thermal-sensitive nanomaterials (MTSN) has become one of the important strategies to improve the therapeutic efficacy. Generally, research has concentrated on developing MW absorption materials for medical frequency bands, such as 424 MHz, 915 MHz, and 2450 MHz.^{15,16} Due to their inherent MW absorption capabilities, these materials have indeed enhanced the effectiveness of hyperthermia treatment to a certain extent. However, the high dielectric constant and high loss characteristics of human tissues, along with the typically sparse distribution of these MW absorbing materials in the tumor region, have limited their practical application effectiveness.¹⁷ Additionally, most studies have focused on the MW absorption capabilities of materials, but have lacked a comprehensive consideration of the tumor microenvironment and tissue polarization characteristics.^{18,19} This has also led to difficulties in achieving effective microwave-thermal sensitization (MTS) for deep-seated tumors. In response to these limitations, this study proposes a new perspective: enhancing the dielectric loss in the local tumor area through the structural properties of materials, rather than solely relying on MW absorption effects.²⁰ We believe that this approach can more effectively promote the deposition of MW power in the tumor area, thereby enhancing the efficacy of MWH.²¹ This strategy not only promises to enhance the MW-thermal response of tumor tissue, but also aims to achieve more precise therapeutic outcomes without increasing damage to healthy tissues. The innovation of this study is that we are not limited to focusing on the MW absorption performance of the material itself, but also adjusting the characteristics of the tumor microdielectric environment through the structural characteristics of the material, thereby improving the MWH effect of the tumor area. This problem-oriented research method can better understand and solve the challenges of existing technologies in deep tumor MWH and bring innovative improvements to the MWH field.

In the field of breast cancer MWH, our team's previously developed conformal-array antenna (CAA) applicator has provided an effective solution for the precise heating of superficial tumors.²⁰ Building upon this foundation, the excitation strategy was further optimized to achieve the heating effect of deep tumors, and the thermal damage score was used to quantitatively analyze the therapeutic effect. Existing studies^{22–24} have demonstrated that the high dielectric loss characteristics of human tissues are key to achieving MWH. However, these characteristics also result in the attenuation of MW energy during deep tumor treatment and the risk of overheating surface tissues. Through the quantitative evaluation of the thermal damage score, we found that although phased array technology can achieve 100% thermal damage of deep tumors, the degree of thermal damage to healthy tissues is unacceptable. In order to surmount these challenges, we

have introduced a novel MTSN, ZIF-8@HA, which, through its distinctive structural features, significantly enhances the dielectric loss in the tumor region. This enhancement subsequently boosts the absorption and thermal conversion efficiency of MW energy. The experimental results show that the MTS effect of ZIF-8@HA is remarkable, and the MW thermal conversion efficiency is as high as 46.46%, which is much higher than our previous research results. The MTS effect of ZIF-8@HA in the phantom is also significant, and the average thermal damage score of healthy tissues has been reduced by more than 10% as determined by coaxial probe measurements and validated through COMSOL simulations. Cellular experiments further substantiated that the combined use of ZIF-8@HA with MW irradiation significantly reduced the survival rate of tumor cells, which was considerably lower than that of other treatment groups. Furthermore, cross-tissue MW heating experiments have confirmed the advantages of using ZIF-8@HA in combination with the CAA. Ultimately, the validation through phantom experiments of ZIF-8@HA integrated with the CAA demonstrated that the incorporation of ZIF-8@HA can significantly accelerate the heating rate in the tumor region, thereby reducing thermal damage to healthy tissues. These results substantiate the significant efficacy and importance of the synergistic application of the CAA with ZIF-8@HA MTSN in MWH for the treatment of subcutaneous deep *in situ* breast cancer.

2. Results and discussion

2.1. The temperature threshold method serves as an evaluation criterion for the CAA applicator

Our MWH research laboratory reported a CAA applicator for the treatment of subcutaneous superficial *in situ* breast cancer tumors²⁰ (Fig. 1). The applicator operates at a frequency of 915 MHz and is composed of 17 circular patch antenna elements, each with a radius of 4 mm, printed on an FR-4 dielectric substrate and excited *via* SMA probe back-feeding. Fig. 1a presents a schematic of the simulated CAA applicator structure, with the main array structure immersed in circulating deionized water. Firstly, the slow-wave effect of deionized water enables miniaturization of the antennas, allowing for the placement of 17 elements around the conformal hemispherical structure with a 48 mm radius. Secondly, the circulating deionized water cools the body's surface layer, promoting

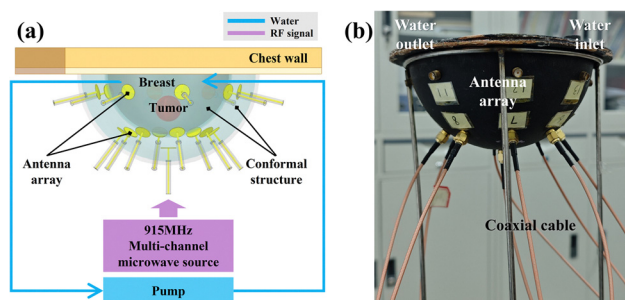


Fig. 1 A 915 MHz 17-element hemispherical CAA applicator. (a) Schematic of the simulation structure. (b) The physical model.



effective deposition of heat in deeper tissues. Fig. 1b shows the physical model of the CAA applicator, which is 3D printed using nylon PA12 material. The casing is embedded with SMA connectors for connection to a coaxial cable, while the inner conductor of the SMA passes through the casing to connect with the circular patch antenna elements. Water inlet and outlet ports are located on both sides of the casing.

The CAA applicator employs time-reversal (TR) technology^{2,10,11,22,25} to optimize the phase of each element in the array.

By using phase conjugation, the signal is fed to each element of the array, achieving an electromagnetic wave enhancement effect at the location of deep tumors. In this study, the thermal damage temperature threshold method was used to evaluate the therapeutic effect.²⁶ This method is based on the calculation model constructed by the direct effect of temperature on the cell survival rate to quantify the degree of thermal damage. At the cellular level, thermal damage is categorized into two forms: necrosis and apoptosis. Necrosis is the process of rapid and passive cell death occurring at extreme temperatures, while apoptosis is a programmed cell death mechanism activated by external high-temperature stimuli.²⁷ It is noteworthy that MWH differs from high-temperature thermal ablation techniques in the mechanisms that induce cell death; the former primarily achieves therapeutic effects by promoting apoptosis rather than directly causing necrosis through high temperatures. According to the literature^{27,28} and clinical experience, human tissue cells undergo apoptosis after being continuously exposed to a temperature of 43 °C for 30 minutes, while necrosis typically occurs at temperatures exceeding 80 °C. Therefore, the thermal damage temperature threshold method defines three key parameters: damage temperature (T_d), which is the temperature threshold at which tissue begins to undergo apoptosis; damage time (t_d), which indicates that maintaining the tissue at a temperature above T_d for a duration of t_d will lead to cell apoptosis; and necrosis temperature (T_n), which is the temperature threshold at which tissue undergoes necrosis. This study focuses on the temperature range between T_d and T_n , specifically the temperature interval between the critical points of apoptosis and necrosis. To accurately quantify the degree of thermal damage to tissue, we introduce the thermal damage score (θ):

$$\theta = \begin{cases} 1, & T > T_n \\ \frac{1}{t_d} \int_0^t (T - T_d) dt, & T_d < T < T_n \end{cases} \quad (1)$$

This study further distinguishes between the tumor domain and the healthy tissue domain by calculating the average thermal damage score for each domain separately. This approach allows us to quantify the effects of thermal therapy under different power inputs by calculating the average thermal damage scores within both domains. The goal is to optimize treatment parameters to maximize tumor damage while minimizing damage to healthy tissue.

The operation method of CAA applicator incentive optimization is as follows:

(1) In the HFSS simulation, the breast is placed in the CAA applicator and a point source is positioned at the tumor location within the breast tissue;

(2) Phase optimization: the HFSS simulation calculates the phase of the signal emitted by the point source as it travels through the breast tissue and deionized water to each array element and applies conjugate processing to the phase information.

(3) Power optimization: COMSOL simulation software is used to calculate the temperature field distribution and the average thermal damage score for the tumor domain and the healthy tissue domain under different input power levels. An optimal power value that achieves 100% thermal damage to the tumor within the treatment time is determined while minimizing thermal damage to healthy tissue.

Fig. 2a illustrates the changes in the temperature field and thermal damage field distribution under different power inputs with a treatment time of 60 minutes. This figure demonstrates the capability of the time-reversal (TR) technique to achieve precise focusing on the target area. As the power increases, the hotspot area expands and effectively deposits energy into the deeper tumor tissue. The thermal damage region also expands with increasing power, gradually fully covering the tumor area.

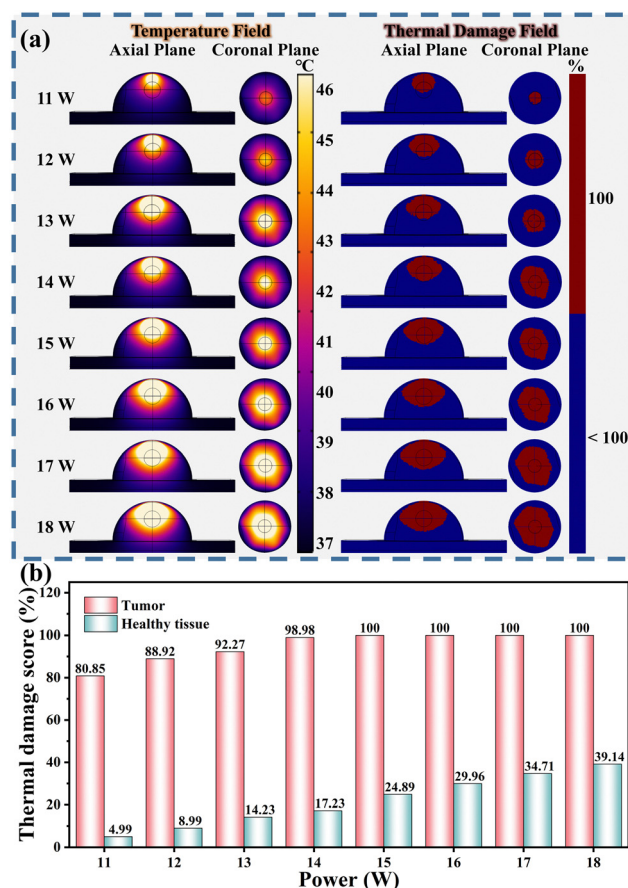


Fig. 2 The distribution of the temperature field and the thermal damage field under different powers. (b) The average thermal damage scores of the tumor domain and healthy tissue domain under different powers.



As shown in Fig. 2b, when the power is set to 15 W, after 60 minutes of treatment, the average thermal damage score for the tumor domain reaches 100%, while the average thermal damage for the healthy tissue domain is at its lowest. If the power is further increased, although it may enhance the thermal damage effect on the tumor, it will also lead to an increase in thermal damage to healthy tissue.

As shown in Fig. 3, the distribution of the temperature field and thermal damage field at different depths (10 mm and 20 mm) was analyzed using the aforementioned excitation optimization method. As shown in Fig. 3(a–d and i), for a 10 mm radius tumor located 10 mm subcutaneously, 7 array elements directly above were activated, each fed with a 6 W power, and heating was applied continuously for 60 minutes. The thermal damage score in the tumor domain just reached 100%, while the average thermal damage score in the healthy tissue domain was 3.08%. In contrast, as shown in Fig. 3(e–h and j), for a tumor of the same size located 20 mm subcutaneously, under the same array configuration, the input power for each array element needed to be increased to 15 W, with continuous heating for 60 minutes, for the average thermal damage score in the tumor domain to just reach 100%. At this point, the average thermal damage score in the healthy tissue domain was 24.89%. By comparing the simulation results for tumors at different depths, it is evident that the CAA applicator can effectively deliver hyperthermia treatment to superficial tumors

while causing minimal thermal damage to surrounding healthy tissues. However, the treatment of deep-seated tumors results in an unacceptable degree of thermal damage to healthy tissues. In light of this challenge in treating deep-seated tumors, we propose an innovative solution in the subsequent chapters: enhancing the dielectric loss in the tumor region by loading ZIF-8@HA nanomaterials, thereby improving the absorption of MW energy and the efficiency of heat conversion in deep-seated tumors.

2.2. Synthesis and characterization of ZIF-8@HA

In this study, ZIF-8 was synthesized *via* a facile one-step self-assembly approach.²⁹ Its morphology was characterized by transmission electron microscopy (TEM) and scanning electron microscopy (SEM) (Fig. 4a and Fig. S1a, ESI[†]). Under TEM, ZIF-8 clearly exhibited a distinct regular cubic structure with sharp edges. In SEM images, ZIF-8 presented regular polyhedral morphology with a uniform particle size of approximately 103 nm. To evaluate the uniformity of the size distribution and stability of the synthesized nanomaterials in solution, we conducted dynamic light scattering (DLS) measurements. The average hydrodynamic diameter of ZIF-8 was approximately 250.46 nm, with a polydispersity index (PDI) of only 0.098 (<0.3) (Fig. 4c). This indicates that the synthesized ZIF-8 nanomaterials have uniform size distribution and good stability. Furthermore, the zeta potential of ZIF-8 was approximately 41.2 mV (Fig. 4e), indicating strong charge repulsion between ZIF-8 particles, which ensures good dispersibility in solution. Hyaluronic acid (HA) was coated onto ZIF-8 through electrostatic interactions in an anhydrous ethanol–water mixed solution.³⁰ ZIF-8 solution and HA solution were mixed at different ratios (w/w). As shown in Fig. S2a (ESI[†]), at a ratio of 20:1, the hydrodynamic diameter increased significantly, and the PDI was >0.3, indicating severe aggregation of ZIF-8 nanoparticles due to HA coating at this ratio. As the mass ratio of ZIF-8 to HA was adjusted from 20:1 to 5:1, the size gradually decreased and stabilized at around 371.46 nm, while the PDI decreased to 0.098 (Fig. 4d). This suggests that at a 5:1 ratio, HA was successfully coated on the ZIF-8 surface, and the size and dispersity of the nanoparticles were optimized. Moreover, as the ZIF-8/HA ratio changed from 20:1 to 5:1, the zeta potential showed a continuous decrease (Fig. S2b, ESI[†]). At a 5:1 ratio, the zeta potential of ZIF-8@HA reversed to −25.7 mV (Fig. 4f). This phenomenon is directly

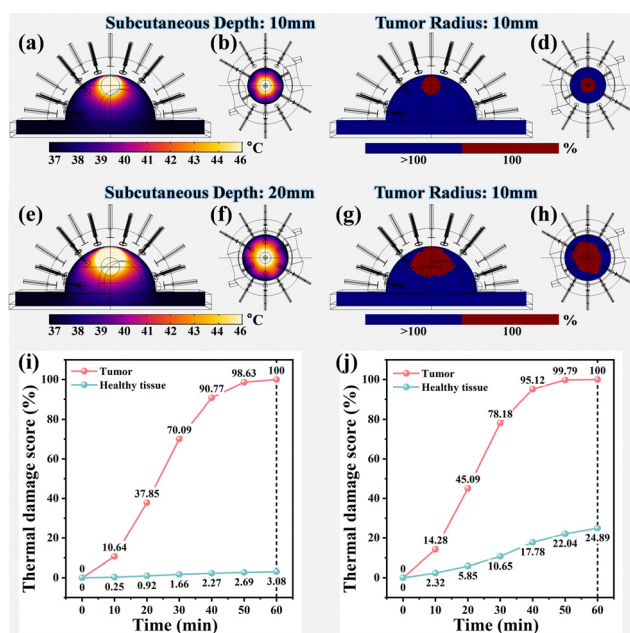


Fig. 3 Simulated temperature and thermal damage fields for the CAA applicator at 10 mm and 20 mm depths. The 10 mm radius tumor at a 10 mm subcutaneous depth: (a) and (b) temperature fields in axial and coronal planes and (c) and (d) thermal damage fields in axial and coronal planes. The 10 mm radius tumor at a 20 mm subcutaneous depth: (e) and (f) temperature fields in axial and coronal planes and (g) and (h) thermal damage fields in axial and coronal planes. Time-varying curves of thermal damage scores in healthy and tumor tissue domains for the: (i) 10 mm depth and (j) 20 mm depth.

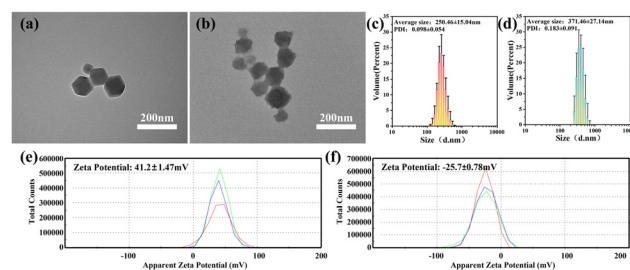


Fig. 4 Characterization of ZIF-8 and SIM@ZIF-8@HA. (a) and (b) TEM images, (c) and (d) hydrodynamic size distributions, and (e) and (f) zeta potential distributions of ZIF-8 and ZIF-8@HA.



attributed to the negative charge properties of HA, confirming the successful coating of HA on the ZIF-8 surface and the consequent significant change in the surface charge state of the nanoparticles. Furthermore, TEM images visually confirmed the uniform coating of HA on the ZIF-8@HA surface (Fig. 4b). SEM images revealed that the coated ZIF-8@HA maintained its polyhedral morphology with a smoother surface (Fig. S2b, ESI†).

2.3. MTS effects of ZIF-8 and ZIF-8@HA *in vitro*

To evaluate the MTS effect of ZIF-8 and its derivative ZIF-8@HA *in vitro*, we conducted a series of MW heating experiments. It is well known that heating induced by MW irradiation is primarily due to the heat generated by the friction of water molecules or ions in the electromagnetic field. Since physiological saline is a solution with components similar to human tissue fluid, it is commonly used as a test medium in the literature.^{15,29} As shown in Fig. 5a and b, different concentrations of ZIF-8 (3, 5, 7, and 10 mg mL⁻¹) were dispersed in physiological saline (0.9% NaCl) and irradiated with MW at a 1.8 W power and 915 MHz frequency for 5 minutes. The results showed that as the concentration of ZIF-8 increased, the temperature of the solution rose to 47.2, 50.3, 58.5, 61.3, and 62.7 °C, respectively. Meanwhile, the control group without ZIF-8 addition showed a temperature increase of only 21.7 °C under the same conditions, which was significantly lower than the experimental groups. This difference indicates that ZIF-8 has a significant MTS effect, which enhances as the concentration increases.

Moreover, after experiencing three cycles of MW heating, ZIF-8 exhibited almost identical heating curves (Fig. 5c), demonstrating its excellent MW-thermal stability.

Furthermore, we evaluated the MW heating performance and MW-thermal stability of ZIF-8@HA. Under the same experimental conditions, the heating effect of ZIF-8@HA was equally satisfactory. As shown in Fig. 5d and e, ZIF-8@HA solutions at 3, 5, 7, and 10 mg mL⁻¹ exhibited temperature increases of 27.9, 31, 35, and 36.9 °C, respectively, under MW irradiation. The data indicate that ZIF-8@HA can also achieve effective temperature elevation under MW irradiation, with the heating effect enhancing as the concentration increases. Moreover, as shown in Fig. 5f, ZIF-8@HA demonstrated good stability during cyclic heating periods. To more intuitively display the temperature changes during the heating process, we used an infrared thermal imaging camera to record the temperature changes in the solution every half minute, with results shown in Fig. 5g. Additionally, we calculated the MW thermal conversion efficiency (η) of ZIF-8 and ZIF-8@HA dispersed in 0.9% NaCl to be 46.87% and 46.46%, respectively (Table S1, ESI†), values that far exceed our previous research results (Fig. 5h).^{31,32} These results collectively demonstrate that both ZIF-8 and ZIF-8@HA possess ideal MTS effects and thermal stability, making them suitable as the MTSN for MWH in breast cancer treatment.

2.4. MTS effects of ZIF-8@HA in a phantom

MW heating experiments were conducted on ZIF-8@HA nanoparticles in a phantom with the same dielectric constant as the human body^{33,34} to evaluate the MTS performance of ZIF-8@HA under simulated human electromagnetic environment conditions. The experiment used a 915 MHz microstrip circular patch antenna to irradiate phantoms loaded with different concentrations (0, 10, 20, and 30 mg mL⁻¹) of ZIF-8@HA. The MW irradiation powers were 5, 10, and 15 W, respectively, with an irradiation time of 15 minutes (Fig. 6a–c). During the experiment, an infrared thermal imaging camera was used to monitor the temperature changes of the phantom models in real-time (Fig. 6e). The experimental results show that as the concentration of ZIF-8@HA increases, the heating effect in the phantoms significantly improves. Under a 5 W irradiation power, the control phantom without ZIF-8@HA experienced a temperature increase of 6.1 °C, while the 30 mg mL⁻¹ ZIF-8@HA group reached a temperature increase of 10.7 °C. Similarly, under 10 W and 15 W powers, similar trends were observed. For ZIF-8@HA concentrations ranging from 10 mg mL⁻¹ to 30 mg mL⁻¹, the temperature rise increased from 18.7 °C to 25.7 °C (10 W) and from 24.5 °C to 34.2 °C (15 W), indicating a positive correlation between the ZIF-8@HA concentration and the MTS effect. Furthermore, the temperature rise curve data reveal the impact of irradiation time on the MTS effect. As the irradiation time increases, the heating effect in the phantoms becomes more pronounced, indicating that the irradiation time is a crucial factor affecting the MTS effect. Under different power conditions, temperature difference analysis between ZIF-8@HA phantoms and the control group shows that the temperature difference between the 30 mg mL⁻¹ ZIF-8@HA phantom and the control group is

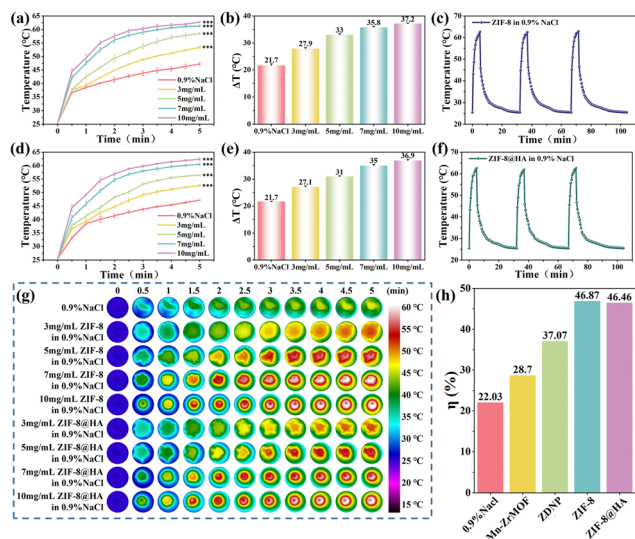


Fig. 5 (a) *In vitro* heating curves of ZIF-8 at different concentrations (0, 3, 5, 7, and 10 mg mL⁻¹) in physiological saline. (b) Temperature change ΔT (°C) at different concentrations based on (a). (c) Cyclic heating curves of ZIF-8 solution. (d) *In vitro* heating curves of ZIF-8@HA at different concentrations (0, 3, 5, 7, and 10 mg mL⁻¹) in physiological saline. (e) Temperature change ΔT (°C) at different concentrations based on (d). (f) Cyclic heating curves of ZIF-8@HA solution. (g) Infrared thermal images of ZIF-8 and ZIF-8@HA at different concentrations under MW irradiation. (h) Comparison of the MW-thermal conversion efficiency of ZIF-8 and ZIF-8@HA nanomaterials with previously reported values for the Mn-ZrMOF and ZDNP (all at 10 mg mL⁻¹ nanomaterial dispersed in physiological saline, a MW radiation power of 1.8 W for 5 min).



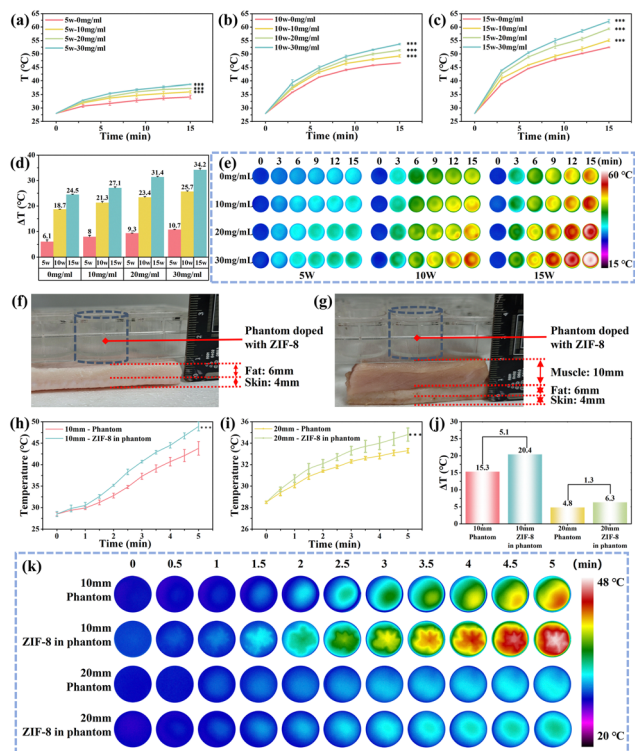


Fig. 6 Temperature rise curves of phantoms with different concentrations of ZIF-8@HA under MW irradiation powers of (a) 5 W, (b) 10 W, and (c) 15 W. (d) Temperature change ΔT ($^{\circ}\text{C}$) based on (a–c). (e) A schematic diagram of infrared thermal imaging temperature changes based on (a–c). MW-thermal sensitization effect experiments on phantoms across (f) 10 mm and (g) 20 mm tissues. Comparison of temperature rise curves for phantoms with different concentrations of ZIF-8@HA across (h) 10 mm and (i) 20 mm tissues. (j) Temperature change ΔT ($^{\circ}\text{C}$) based on (h–i). (k) A schematic diagram of infrared thermal imaging temperature changes based on (h–i).

4.6 $^{\circ}\text{C}$; when the power is increased to 10 W, the temperature difference increases to 7 $^{\circ}\text{C}$; further increasing the power to 15 W expands the temperature difference to 9.7 $^{\circ}\text{C}$. This result indicates that as the MW power increases, the MTS effect of ZIF-8@HA-loaded phantoms significantly enhances compared to the control pure phantoms. Considering the three factors of concentration, time, and power comprehensively, the experimental results clearly indicate that ZIF-8@HA, as an MTSN, demonstrates significantly enhanced MTS effects in phantoms with electromagnetic environments identical to the human body as the concentration increases, irradiation time extends, and irradiation power rises.

To investigate the deep heating efficacy of ZIF-8@HA as an MTSN, we designed a series of cross-tissue MW heating experiments using phantoms. In the experimental design, *ex vivo* porcine tissues (skin, fat, and muscle) of varying thicknesses were placed between the MW irradiation source and the phantoms, constructing tissue models with thicknesses of 10 mm (skin + fat) and 20 mm (skin + fat + muscle), respectively (Fig. 6f and g). The experiment compared the heating effects of 0 mg mL^{-1} (control) and 30 mg mL^{-1} ZIF-8@HA under both conditions. It was found that with a 10 mm tissue thickness, the sensitization temperature difference of the 30 mg mL^{-1}

ZIF-8@HA phantom compared to the control group was 5.1 $^{\circ}\text{C}$ (Fig. 6h and j), while when the tissue thickness increased to 20 mm, the sensitization temperature difference decreased to 1.3 $^{\circ}\text{C}$ (Fig. 6i and j). Infrared thermal imaging recorded the temperature changes (Fig. 6k). This phenomenon aligns with the high dielectric loss characteristics of human tissues revealed in previous studies,^{22–24} namely that MW energy rapidly attenuates when penetrating deep tissues, leading to reduced MW power density in deep tissues, which in turn affects the MTS effect. Furthermore, the experimental results emphasize the potential advantages of the CAA in MWH. The CAA can achieve superposition of multi-element electromagnetic fields, thereby realizing stronger power-targeted deposition in deep tissues. This characteristic is particularly beneficial for the use of MTSN, as it can improve the heating efficiency of deep tissues, thereby enhancing the MTS effect.

2.5. Mechanism analysis of MTS

Further analysis of the MTS mechanism of ZIF-8@HA was performed. The N_2 isothermal adsorption-desorption results show that the specific surface area of ZIF-8@HA is 1459.89 $\text{m}^2 \text{g}^{-1}$ (Fig. 7a), with an average micropore diameter of approximately 7.3 \AA (Fig. 7b). The high specific surface area of ZIF-8@HA and its extensive contact with the medium can enhance interfacial polarization, thereby significantly increasing the dielectric loss (ϵ''). This effect is particularly pronounced in areas where ZIF-8@HA is densely distributed, leading to an increase in dielectric loss in the local tumor region. Moreover, the rich porous structure of ZIF-8@HA provides abundant adsorption sites, capable of adsorbing nearby ions to form a confinement effect.^{24,29,35} During MW irradiation, ions undergo Brownian motion, and ZIF-8@HA constrains these ions within a limited space, causing their collisions to become more intense and frequent. This accelerates the efficient conversion of MW energy into thermal energy, further enhancing the dielectric loss. Using phantoms with electrical parameters matching those of human tissues as an ideal platform to simulate the *in vivo* environment, ZIF-8@HA at different concentrations was dispersed in the phantoms (Fig. 7c). Based on this, the coaxial probe method was used to evaluate the effect of ZIF-8@HA loading on the dielectric loss of the phantoms (Fig. 7d). This experimental design not only simulates the real electromagnetic environment conditions in biological media, but also allows the direct measurement of the effect of material loading on dielectric loss, thus providing a more comprehensive and precise investigation of the MTS mechanism. As shown in Fig. 7e and f, measurements using the coaxial probe method clearly demonstrate that as the concentration of ZIF-8@HA increases, the dielectric loss (ϵ'') of the phantoms shows a significant upward trend. This result directly reveals a positive correlation between the ZIF-8@HA concentration and the dielectric loss.

Inputting the measured results into the COMSOL CAA simulation model, the results visually demonstrate that as the ZIF-8 concentration increases (*i.e.*, as the imaginary part of the dielectric constant ϵ'' increases), the time required for the



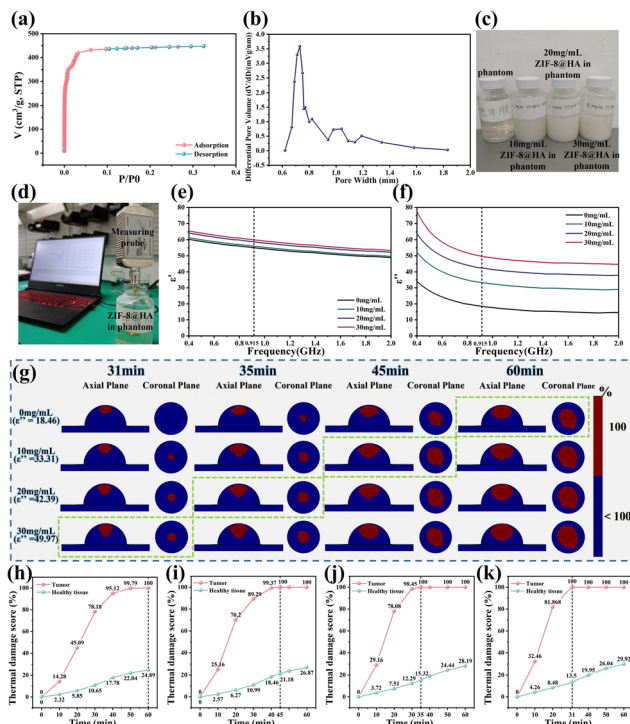


Fig. 7 The (a) specific surface area and (b) average micropore diameter of ZIF-8@HA from N_2 isothermal adsorption–desorption. (c) Phantoms with varying ZIF-8@HA concentrations. (d) The dielectric property measurement of ZIF-8@HA-loaded phantoms using the coaxial transmission line method. (e) Dielectric constant ϵ' and (f) dielectric loss ϵ'' of phantoms with different ZIF-8@HA concentrations. (g) COMSOL simulations: the thermal damage distribution for various ZIF-8@HA concentrations. COMSOL simulations: time-dependent average thermal damage scores in healthy and tumor domains for (h) 0 mg mL^{-1} , (i) 10 mg mL^{-1} , (j) 20 mg mL^{-1} , and (k) 30 mg mL^{-1} ZIF-8@HA.

tumor domain to reach 100% thermal damage significantly shortens. Meanwhile, the average thermal damage score in the healthy tissue domain also decreases. This series of results quantitatively illustrates the potential of ZIF-8 as an MTSN in improving MWH efficiency and reducing damage to healthy tissues. Fig. 7g demonstrates a representative case study: for a tumor with a radius of 10 mm located 20 mm beneath the skin surface, we activated 7 array elements directly above the tumor region. Each element was supplied with 15 W power under continuous heating conditions.

Without ZIF-8@HA ($\epsilon'' = 18.46$), 60 minutes of heating is required for the tumor domain to reach 100% thermal damage, at which point the average thermal damage score in the healthy tissue domain is 24.89% (Fig. 7h). When the ZIF-8@HA concentration is 10 mg mL^{-1} ($\epsilon'' = 33.31$), the tumor domain reaches 100% thermal damage within 45 minutes, and the average thermal damage score in the healthy tissue domain decreases to 21.18% (Fig. 7i). At a ZIF-8@HA concentration of 20 mg mL^{-1} ($\epsilon'' = 42.39$), the tumor domain requires only 35 minutes to reach 100% thermal damage, and the average thermal damage score in the healthy tissue domain further decreases to 15.32% (Fig. 7j). At the highest concentration of 30 mg mL^{-1} ($\epsilon'' = 49.97$), the tumor domain reaches 100% thermal damage

within 31 minutes, and the average thermal damage score in the healthy tissue domain is only 13.5%, which is a reduction of 11.39% compared to when ZIF-8@HA is not loaded (Fig. 7k).

2.6. Cytotoxicity and *in vitro* therapeutic effect of ZIF-8@HA

Quantitative analysis of the cytotoxicity of ZIF-8 and its HA-modified derivative, ZIF-8@HA nanomaterials, was conducted using the MTT assay. Mouse embryonic fibroblasts (L929) and mouse breast cancer cells (4T1) were selected as model cell lines for the experiment. These cells were co-incubated with a series of ZIF-8 and ZIF-8@HA nanomaterials at various concentrations for 12 hours. Subsequently, cell viability was determined using the MTT reagent to assess the cytotoxicity of the materials. The experimental data revealed that after 12 hours of incubation with L929 cells at various concentrations of ZIF-8@HA, the cell viability remained at 76% even at the highest concentration (100 $\mu\text{g mL}^{-1}$), indicating low cytotoxicity (Fig. 8a). For 4T1 cells under the same concentration conditions, the cell viability was maintained at 85%, further confirming the low toxicity profile of ZIF-8@HA nanomaterials (Fig. 8b). However, compared to ZIF-8@HA, the unmodified ZIF-8 nanomaterials exhibited higher cytotoxicity. Under identical incubation conditions with L929 fibroblasts and 4T1 breast cancer cells, ZIF-8 significantly reduced cell viability even at lower concentrations (Fig. 8a and b). These results suggest that the HA-modified ZIF-8 nanomaterials (*i.e.*, ZIF-8@HA) demonstrated a notable reduction in cytotoxicity.

Given the excellent MTS performance of ZIF-8@HA in physiological saline and phantoms, as well as its low cytotoxicity profile, we further investigated its efficacy in *in vitro* cellular MWH. This study employed mouse 4T1 breast cancer cells for *in vitro* MWH experiments to evaluate the anti-tumor capability of ZIF-8@HA nanomaterials combined with MW irradiation under *in vitro* conditions. In the study, 4T1 tumor cells were first co-incubated with ZIF-8@HA nanomaterials for 12 hours, ensuring effective intracellular internalization and accumulation of ZIF-8@HA through cellular endocytosis mechanisms. Subsequently, unabsorbed materials in the culture medium were removed. The cells were then exposed to 915 MHz MW radiation at a power of 1.8 W for 3 minutes. The temperature change curves during heating (Fig. 8d) showed that ZIF-8@HA combined with the MW radiation group (MW + ZIF-8@HA group) exhibited a more

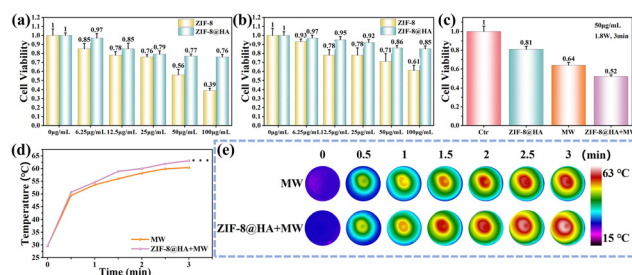


Fig. 8 The MTT cytotoxicity assay for (a) 4T1 cells and (b) L929 cells. (c) *In vitro* treatment experiments with 4T1 cells. (d) Temperature rise curves during treatment. (e) Thermal infrared imaging.



significant MTS effect compared to the MW radiation alone group (MW group), which was visually demonstrated in the infrared thermal imaging (Fig. 8e). Quantitative analysis of cell viability (Fig. 8c) further confirmed the positive role of ZIF-8@HA nanomaterials in MWH: the cell viability was 81% with MW irradiation alone (MW group) and 64% with ZIF-8@HA treatment alone (ZIF-8@HA group), while under combined treatment of ZIF-8@HA and MW irradiation (MW + ZIF-8@HA group), the cell viability significantly decreased to 52%. This result indicates that under MWH conditions, ZIF-8@HA nanomaterials can significantly enhance the thermal sensitivity of tumor cells, demonstrating good anti-tumor efficacy.

2.7. Experimental verification of CAA synergistic ZIF-8@HA

To validate the actual MWH effect of ZIF-8@HA nanomaterials combined with the CAA applicator, experiments were conducted using phantoms. Fig. 9a illustrates the experimental design for CAA synergistic ZIF-8@HA phantom heating. A 3-channel fiber-optic temperature sensor (FTM-3CH-C220, Beijing Oriental Ruizer Technology Co., Ltd, China) was inserted into the phantom to record real-time temperature changes during heating. As shown in Fig. 9b, to accurately simulate the tumor region loaded with materials, phantoms containing

different concentrations (0 mg mL^{-1} and 30 mg mL^{-1}) of ZIF-8@HA were injected into thin plastic spherical shells. A PVC thin rigid pipe was used to connect and secure the shells, facilitating fixture with an iron stand and precise positioning of temperature measurement fibers. The fixation of temperature measurement fibers and positioning of measurement points are depicted in Fig. 9c. The PVC thin rigid pipe guided the fibers, and an iron stand secured them, enabling the precise localization of temperature measurement points. The three finalized temperature measurement points were: point A: located at the center of the tumor interior, with a tumor radius of 25 mm and a depth set at 20 mm; points B and C: positioned 5 mm from either side of the tumor. The experimental setup is shown in Fig. 9d. The main body of the CAA Applicator was placed in a 37°C thermostatic chamber (DHG-9310A, Beijing Luxi Technology Co., Ltd, China) to simulate human body temperature conditions. Deionized water was filled into the CAA applicator using a circulating water bath (HH-501, Baita Xinbao Instrument Factory, China). The output of a 915 MHz high-power MW source was connected to a 6-way power divider to achieve uniform distribution of MW energy across six channels. Phase delays were implemented through coaxial cables of varying lengths for the six outputs.

The heating duration was determined by the thermal damage score (θ) reaching 100% at the target area measurement point. Real-time temperature monitoring *via* fiber-optics considered 43°C as the thermal damage temperature (T_d) for the target area. Heating continued for an additional 30 minutes (t_d) to achieve a 100% thermal damage score, at which point heating was terminated. Fig. 10a shows the temperature–time curves for points A, B, and C without ZIF-8@HA nanomaterial loading. Point A (tumor center) reached 43°C after 29 minutes of heating, attaining the thermal damage temperature threshold (T_d), followed by 30 minutes (t_d) of additional heating. In contrast, for the group loaded with 30 mg mL^{-1} ZIF-8@HA nanomaterials (Fig. 10c), point A rapidly reached 43°C within 11 minutes. After 30 minutes of continued heating, the thermal damage score reached 100% at 41 minutes, reducing the total heating time by

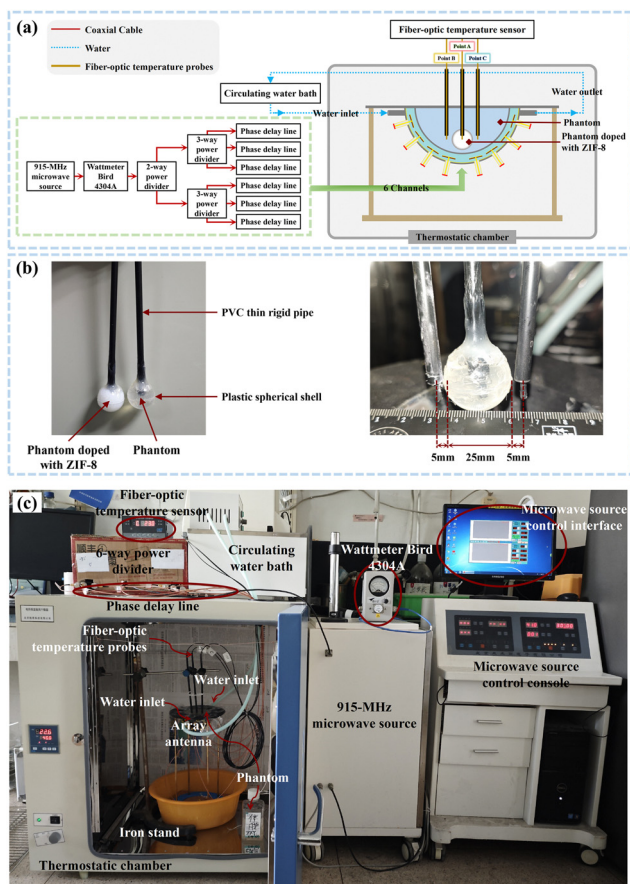


Fig. 9 (a) A schematic diagram of the experiment. (b) The fiber-optic temperature measurement method and measurement points. (c) The experimental setup.

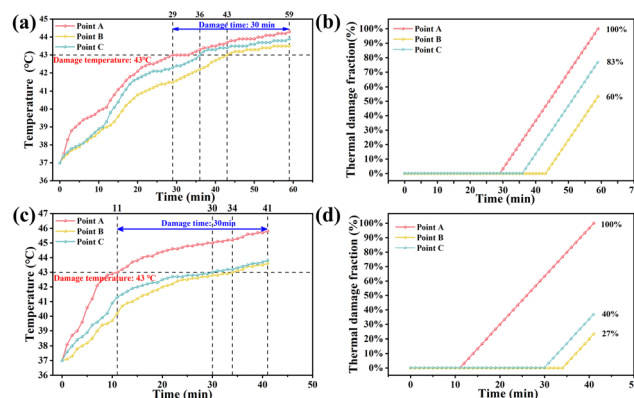


Fig. 10 (a) Temperature and (b) thermal damage score curves without ZIF-8@HA loading. (c) Temperature and (d) thermal damage score curves with 30 mg mL^{-1} ZIF-8@HA loading.



20 minutes. To visualize the thermal damage scores, Fig. 10b and d present the time-dependent thermal damage score curves based on the temperature data from Fig. 10a and c. For the group without ZIF-8@HA nanomaterials, when heating stopped at 59 minutes, the thermal damage scores for points B and C were 83% and 60%, respectively (Fig. 10b). In the ZIF-8@HA nanomaterial-loaded group, due to significantly enhanced heating rates in the tumor area, the thermal damage scores for points B and C were 40% and 27%, respectively, when heating ceased at 41 minutes, representing reductions of 43% and 33% compared to the former group.

The experimental results demonstrate that the combination of ZIF-8@HA nanomaterials with the CAA applicator significantly enhances the efficiency and precision of MWH. By accelerating the heating rate in the tumor region, this approach not only substantially reduces the duration of thermal therapy but also effectively minimizes thermal damage to surrounding healthy tissues. These findings affirm the significant advantages and clinical application potential of this synergistic treatment in MWH.

3. Experimental

3.1. Simulation of the CAA applicator

In this study, we used Ansys HFSS 2018 to perform electromagnetic simulation modeling of the CAA applicator, aiming to calculate the phase information of each array element in TR technology. To simulate an open free space environment, the CAA applicator was placed at the center of an air box, with its outer surface set at a distance of one-quarter wavelength from the applicator. The boundary of the air box was set as a radiation boundary condition. For the electromagnetic characteristic analysis, we employed the finite element method (FEM) and used the driven modal solution type.

To further analyze the distribution of temperature and thermal damage fields, we conducted coupled electromagnetic and thermal simulations using COMSOL Multiphysics 5.5. In the RF module, all domains of the CAA applicator and homogeneous breast model were selected, with conditions set consistent with those in HFSS. In the bioheat transfer module, the biological tissue domain of the homogeneous breast model was selected. The initial temperature was set to normal human body temperature (37 °C). To simulate a circulating environment of 37 °C deionized water, a 37 °C temperature boundary condition was applied to the outer surface of the breast skin, while other external surfaces were set as thermally insulated boundaries. The coupling of electromagnetic effects and heat transfer processes was achieved through the electromagnetic-heat multiphysics interface. The RF module used a frequency-domain stationary solver to resolve electromagnetic problems, while the bioheat transfer module employed a transient time solver to handle heat transfer issues.

3.2. Materials

Sodium chloride (NaCl), anhydrous methanol, and anhydrous ethanol were purchased from Beijing Chemical Reagent

Company (China). Zinc nitrate ($\text{Zn}(\text{NO}_3)_2 \cdot 6\text{H}_2\text{O}$) was supplied by Tianjin Chemical Reagent 3 Plant. 2-Methylimidazole (2MI) was purchased from Beijing Bailingwei Technology Co., Ltd. Hyaluronic acid (HA) was purchased from Beijing Lanyi Reagent Company (China). Sucrose was obtained from Tianjin Fuchen Chemical Reagent Co., Ltd. Hydroxyethyl cellulose was purchased from Shanghai Macklin Biochemical Technology Co., Ltd. NaCl was obtained from Sinopharm Chemical Reagent Co., Ltd. The reagents used in this work were of analytical grade (A.R.) and required no further purification.

3.3. Preparation and characterization of materials

In this experiment, ZIF-8 was synthesized using a one-step self-assembly method. First, $\text{Zn}(\text{NO}_3)_2 \cdot 6\text{H}_2\text{O}$ (0.446 g) and 2MI (0.513 g) were separately dispersed in methanol (25 mL). Then, the 2 MI methanol solution was added to the $\text{Zn}(\text{NO}_3)_2 \cdot 6\text{H}_2\text{O}$ methanol solution. The mixture was allowed to react at room temperature for 24 hours, during which the colorless clear solution gradually turned milky white. The clear supernatant was removed using a pipette, followed by centrifugation to obtain the solid precipitate ZIF-8. The precipitate was washed three times with anhydrous ethanol by centrifugation. HA was coated onto ZIF-8 through electrostatic interactions in an anhydrous ethanol-water mixed solution. First, HA (10 mg) was dissolved in water (2 mL), and 10 μL of 1 M NaOH solution was added to adjust the pH. Then, ZIF-8 (50 mg) was dissolved in anhydrous ethanol (2 mL). The HA aqueous solution was added dropwise to the ZIF-8 ethanol solution. The mixture was stirred for 15 hours. After washing three times with anhydrous ethanol, the nanomaterial ZIF-8@HA was successfully obtained.

The morphology of the obtained ZIF-8 and ZIF-8@HA was characterized using transmission electron microscopy (TEM, HT7700, Hitachi, Japan) and scanning electron microscopy (SEM, Model 4300, Hitachi, Japan). The hydrodynamic particle size distribution and zeta potential were measured using a Zeta-sizer (Malvern Instruments Zeta-sizer Nano ZS90, UK). The specific surface area and pore size of ZIF-8@HA were determined using a specific surface area and pore size analyzer (V-Sorb 2800P, Beijing Jin'aipu Technology Co., Ltd, China).

3.4. MTS effect tests

MTS effect tests were divided into two parts, the *in vitro* MTS effect and the phantom MTS effect, to evaluate the performance of ZIF-8 and ZIF-8@HA as the MTSN.

3.4.1. *In vitro* MTS effect. First, ZIF-8 and ZIF-8@HA were dispersed in 0.9% NaCl at different concentrations of 0, 3, 5, 7, and 10 mg mL^{-1} . To ensure uniform dispersion, each sample was treated in an ultrasonic bath for 5 minutes. The treated dispersions were transferred to wells of a 12-well cell culture plate, and 1 mL of the sample was added to each well. The MW irradiation antenna was positioned beneath the cell culture plate, while an infrared thermal imaging camera was installed directly above to monitor the temperature changes of the samples in real-time. The samples were exposed to MW irradiation at a frequency of 915 MHz and a power of 1.8 W for a duration of 5 minutes, with temperature data recorded every



30 seconds. Additionally, to verify the thermal stability of the materials, the samples underwent three cycles of MW heating, with temperature changes recorded after each heating cycle.

3.4.2. Phantom MTS effect. This experiment used a phantom formulation reported in the literature,^{33,34} consisting of 54% water, 1.4% NaCl, 45% sucrose, 1% hydroxyethyl cellulose (HEC), and 0.1% bactericide. ZIF-8@HA at different concentrations (0, 10, 20, and 30 mg mL⁻¹) was dispersed in the phantom. Each sample was treated in an ultrasonic bath for 5 minutes, then transferred to a well of a 12-well cell culture plate, and 2 mL of the sample was added to each well. Subsequently, the phantom was subjected to MW irradiation using a 915 MHz microstrip circular patch antenna, with irradiation powers set at 5, 10, and 15 W for a duration of 15 minutes, and temperature data were recorded every 3 minutes. An infrared thermal imager was used to monitor and record the temperature changes of the phantom in real-time. Furthermore, to investigate the MTS effect in deep cross-tissue scenarios, we placed *ex vivo* porcine tissues of different thicknesses (including skin, fat, and muscle) between the MW irradiation source and the phantom, constructing cross-tissue models of 10 mm and 20 mm thicknesses.

Each experiment was repeated three times to ensure the accuracy and reliability of the data. The data were analyzed using statistical software to evaluate the efficacy of ZIF-8 and ZIF-8@HA as the MTSN.

3.5. Electromagnetic test

3.5.1 Coaxial probe method (Sainty-Tech Communications Limited R60, China). First, ZIF-8@HA was dispersed in the phantom at different concentrations and uniformly dispersed using an ultrasonic bath. Subsequently, the phantom sample was placed at the open end of the coaxial probe, ensuring good contact between the probe and the sample while avoiding the formation of bubbles. The electromagnetic properties of the ZIF-8@HA phantom were measured using the coaxial probe method.

3.6. *In vitro* cytotoxicity assay

The *in vitro* cytotoxicity experiment was conducted using the MTT (methyl thiazolyl tetrazolium) colorimetric assay. Mouse embryonic fibroblasts (L929) and mouse breast cancer cells (4T1) were selected as model cell lines for the experiment. Cells were seeded in 96-well culture plates at a density of 1×10^4 cells per well and cultured for 24 hours at 37 °C with 5% CO₂ to form a monolayer. Subsequently, the cells were co-cultured with a series of gradient concentrations of ZIF-8 and ZIF-8@HA nanomaterials (0, 6.25, 12.5, 25, 50, and 100 µg mL⁻¹). After 12 hours of co-culture, MTT solution (0.5 mg mL⁻¹) was added to each well and incubated for an additional 4 hours. MTT solution can be reduced by mitochondrial dehydrogenases in living cells to form purple formazan crystals, the production of which is proportional to cell viability. After incubation, the MTT solution was carefully removed from the culture wells and replaced with 150 µL of dimethyl sulfoxide (DMSO) to dissolve the formed formazan crystals. Finally, the absorbance (OD) of each well

was measured at 490 nm using a microplate reader. Wells containing cells without nanomaterials served as negative controls to determine 100% cell viability. Ten replicate wells were set up for each concentration group to ensure data accuracy and reproducibility.

3.7. *In vitro* tumor cell inhibition experiment

The *in vitro* tumor inhibition effect of ZIF-8@HA nanomaterials was studied using the 4T1 cell model. The experiment was divided into four groups: (1) control group, receiving no treatment; (2) MW group, receiving only MW radiation; (3) ZIF-8@HA group, only adding ZIF-8@HA nanomaterials (50 µg mL⁻¹); (4) ZIF-8@HA + MW group, first adding ZIF-8@HA nanomaterials (50 µg mL⁻¹), followed by MW radiation. 4T1 cells were seeded in 6-well plates at a density of 1×10^5 cells per well and cultured in RPMI 1640 medium containing 10% fetal bovine serum at 37 °C with 5% CO₂ for 24 hours to ensure cell adherence and growth. Subsequently, 50 µg mL⁻¹ ZIF-8@HA was added to groups (2) and (4) and incubated for an additional 12 hours. Thereafter, cells in the MW and ZIF-8@HA + MW groups were subjected to MW radiation (power 1.8 W, duration 3 minutes). After MW treatment, cells were transferred to 96-well plates and incubated for 12 hours. Finally, the cell viability in each group was assessed using the MTT assay.

3.8. CAA synergistic ZIF-8@HA experiment

The CAA Applicator and the phantom were placed in a thermostatic chamber (DHG-9310A, Beijing Luxi Technology Co., Ltd, China) to simulate constant human body temperature conditions and reduce the influence of external temperature fluctuations on experimental results. The design of the thermostatic chamber allowed for circulating water tubes, temperature measurement optical fibers, and coaxial cables to pass through its holes. The holes were sealed with insulating gaskets to ensure temperature uniformity within the chamber.

3.8.1. Before experiment commencement. The thermostatic chamber door was closed and set to 37 °C. The heating experiment was initiated after the 3-channel fiber-optic temperature sensor (FTM-3CH-C220, Beijing Oriental Ruizer Technology Co., Ltd, China) monitoring confirmed that the phantom temperature had stabilized at 37 °C ± 0.5 °C.

3.8.2. During the heating experiment. Deionized water was circulated through the applicator at a flow rate of 50 mL s⁻¹ using a circulating water bath (HH-501, Baita Xinbao Instrument Factory, China). A 915 MHz high-power MW source (KY-300, Nanjing Kangyou Microwave Energy Application Research Institute, China) distributed MW energy evenly to six input ports of the applicator through a six-way power divider (CP06, Sanjwot Communications Co., Ltd, China, operating frequency range: 800–37 000 MHz). Phase delays at each port were achieved using coaxial cables of different lengths. The actual input power and the phase to the applicator were determined based on the excitation optimization calculations in Section 2.1. The heating duration was targeted to achieve a thermal damage fraction (θ) of 100% at the target area measurement point. Fiber optic temperature sensors continuously monitored the temperature in real-time. When the target area reached



43 °C, it was considered to have reached the damage temperature (T_d). Heating continued for an additional 30 minutes (t_d), at which point 100% thermal damage was deemed to have occurred at this point, and heating was subsequently stopped.

3.9. Statistical analysis

The data are presented as mean \pm standard error, and the statistical significance was determined at a $p < 0.05$. Asterisks (*) denote the level of significance between entries based on the t -test ($p < 0.05$, ** $p < 0.01$, *** $p < 0.001$).

4. Conclusions

This study explores the synergistic MWH effects of combining the CAA applicator with MTSN ZIF-8@HA for the treatment of subcutaneous deep *in situ* breast cancer. Through a series of experimental studies and theoretical analyses, the synthesis and characterization of ZIF-8@HA, its MW thermal conversion efficiency, the MTS mechanism, and the synergistic treatment effect with the CAA applicator were thoroughly investigated. The research results indicate that this synergistic strategy demonstrates significant advantages in improving tumor treatment efficiency and reducing damage to healthy tissues. The main conclusions are as follows:

1. As an MTSN, ZIF-8@HA's unique structural characteristics significantly increased the dielectric loss in the tumor area, enhancing MW energy absorption and thermal conversion efficiency. *In vitro* experiments demonstrated that ZIF-8@HA exhibited a high MW thermal conversion efficiency of up to 46.46%, proving its potential as an MTSN.
2. The phantom MTS effect of ZIF-8@HA was also significant, and through measurements using the coaxial probe method and COMSOL simulations, the average thermal damage score of healthy tissues was reduced by more than 10%.
3. Cell experiments showed that when ZIF-8@HA was used in combination with MW irradiation, the survival rate of tumor cells decreased significantly, far lower than other treatment groups.
4. Cross-tissue MW heating verification experiments also revealed the advantages of combining ZIF-8@HA with the CAA applicator.
5. The combined application of the CAA applicator and ZIF-8@HA significantly improved the precision and efficiency of MWH. Phantom experiment results indicated that this synergistic strategy could significantly shorten the time for the tumor area to reach 100% thermal damage while effectively reducing thermal damage to healthy tissues.

In summary, the combination of the CAA applicator and ZIF-8@HA has demonstrated significant therapeutic effects and clinical application potential in MWH for subcutaneous deep *in situ* breast cancer.

Data availability

The data that support the findings of this study are available from the corresponding author upon reasonable request.

Conflicts of interest

There are no conflicts to declare.

Acknowledgements

This work was supported in part by the National Natural Science Foundation of China (NSFC) under Grant No. 62461048, in part by the NSFC under Grant No. 61961033, in part by the NSFC under Grant No. U20A20335, and in part by the NSFC under Grant No. 62001456.

References

- 1 R. L. Siegel, A. N. Giaquinto and A. Jemal, *Ca-Cancer J. Clin.*, 2024, **74**, 12–49.
- 2 C. Lyu, W. Li, S. Li, Y. Mao and B. Yang, *Sensors*, 2023, **23**, 1051.
- 3 G. Yildiz, I. Farhat, L. Farrugia, J. Bonello, K. Zarb-Adami, C. V. Sammut, T. Yilmaz and I. Akduman, *Sensors*, 2023, **23**, 6592.
- 4 M. Elsaadi and R. Hamad, *Circuits Syst.*, 2023, **14**, 10–18.
- 5 W. Guo, Y. Du, Y. Wang, L. Qin, L. Tan, Y. Zheng, D. Yang and X. Meng, *Mater. Express*, 2020, **10**, 1607–1614.
- 6 N. Nizam-Uddin, W. M. Abdulkawi, I. Elshafiey and A.-F. A. Sheta, *Biomed. Signal Process. Control*, 2022, **71**, 103084.
- 7 M. Zanolli, E. Ek and H. Dobšicek Trefná, *Cancers*, 2023, **15**, 1447.
- 8 M.-A. Damavandi and M. Khalaj-Amirhosseini, *IEEE Antennas Wirel. Propag. Lett.*, 2024, pp. 1488–1492.
- 9 R. Choudhary and K. Arunachalam, *2022 IEEE Region 10 Symposium (TENSYP)*, 2022, pp. 1–3.
- 10 D. Baskaran and K. Arunachalam, *IEEE Trans. Antennas Propag.*, 2020, **69**, 1706–1715.
- 11 F. Rahimi and S. Chamaani, *Microw. Opt. Technol. Lett.*, 2020, **62**, 3754–3766.
- 12 H. A. Elkayal and N. E. Ismail, *Comput. Methods Biomech. Biomed. Eng.*, 2021, **24**, 985–994.
- 13 G. Yildiz, H. Yasar, I. E. Uslu, Y. Demirel, M. N. Akinci, T. Yilmaz and I. Akduman, *Sensors*, 2022, **22**, 6343.
- 14 D. Baskaran and K. Arunachalam, *IEEE Trans. Microwave Theory Tech.*, 2021, **70**, 622–630.
- 15 M. Yu, S. Li, X. Ren, N. Liu, W. Guo, J. Xue, L. Tan, C. Fu, Q. Wu and M. Niu, *ACS Nano*, 2024, **18**, 3636–3650.
- 16 Z. Liu, X. Tan, Y. Huang, W. Li, N. Yang, R. Yuan, Q. Cheng, L. Liu and L. Ge, *Chem. Eng. J.*, 2023, **471**, 144688.
- 17 L. Jin, Y. Zheng, X. Liu, Y. Zhang, Z. Li, Y. Liang, S. Zhu, H. Jiang, Z. Cui and S. Wu, *Small*, 2022, **18**, 2204028.
- 18 L. Jin, X. Liu, Y. Zheng, Y. Zhang, Z. Li, S. Zhu, H. Jiang, Z. Cui and S. Wu, *ACS Nano*, 2023, **17**, 18200–18216.
- 19 H. Zhu, B. Li, X. Liu, Y. Qiao, Y. Lv, Y. Zheng, S. Zhu, Z. Li, Z. Cui and J. Shen, *ACS Nano*, 2022, **16**, 21098–21110.
- 20 J. Gao, Inner Mongolia University of Science and Technology, 2022, DOI: [10.27724/d.cnki.gnmngk.2022.000506](https://doi.org/10.27724/d.cnki.gnmngk.2022.000506)Master.



- 21 E. I. Mohamed, S. M. Abdel-Kader and M. I. Badawi, *2023 International Telecommunications Conference (ITC-Egypt)*, 2023, pp. 219–224.
- 22 I. Androulakis, K. Sumser, M. N. Machielse, L. Koppert, A. Jager, R. Nout, M. Franckena, G. C. van Rhooen and S. Curto, *Int. J. Hyperthermia*, 2022, **39**, 1213–1221.
- 23 M. G. Aram, H. Aliakbarian and H. D. Trefná, *Microw. Opt. Technol. Lett.*, 2021, **63**, 3086–3091.
- 24 J. Song, X. Sun, Y. Du, Q. Wu, M. Niu, C. Fu, L. Tan, X. Ren, L. Chen and X. Meng, *ACS Appl. Bio Mater.*, 2022, **5**, 4154–4164.
- 25 A. Dadzadi and R. Faraji-Dana, *2019 IEEE Asia-Pacific Microwave Conference (APMC)*, 2019, pp. 1107–1109.
- 26 C. Chen, M.-A. Yu, L. Qiu, H.-Y. Chen, Z.-L. Zhao, J. Wu, L.-L. Peng, Z.-L. Wang and R.-X. Xiao, *Appl. Sci.*, 2021, **11**, 8271.
- 27 M. Payne, S. H. Bossmann and M. T. Basel, *Wiley Interdiscip. Rev.: Nanomed. Nanobiotechnol.*, 2020, **12**, e1638.
- 28 P. S. Yarmolenko, E. J. Moon, C. Landon, A. Manzoor, D. W. Hochman, B. L. Viglianti and M. W. Dewhirst, *Int. J. Hyperthermia*, 2011, **27**, 320–343.
- 29 Q. Wu, M. Li, L. Tan, J. Yu, Z. Chen, L. Su, X. Ren, C. Fu, J. Ren and L. Li, *Nanoscale Horiz.*, 2018, **3**, 606–615.
- 30 E. A. M. S. Obaid, S. Wu, Y. Zhong, M. Yan, L. Zhu, B. Li, Y. Wang, W. Wu and G. Wang, *Biomater. Sci.*, 2022, **10**, 4837–4847.
- 31 C. Fu, H. Zhou, L. Tan, Z. Huang, Q. Wu, X. Ren, J. Ren and X. Meng, *ACS Nano*, 2017, **12**, 2201–2210.
- 32 T. Li, Q. Wu, W. Wang, Z. Chen, L. Tan, J. Yu, C. Fu, X. Ren, P. Liang and J. Ren, *Biomaterials*, 2020, **234**, 119773.
- 33 Y. Wang, S. Yan and B. Huang, *IEEE Trans. Antennas Propag.*, 2022, **70**, 6537–6550.
- 34 W. Lei and Y.-X. Guo, *IEEE Trans. Antennas Propag.*, 2018, **66**, 5706–5715.
- 35 X. Zhu, C. He, L. Tan, X. Qi, M. Niu, X. Meng and H. Zhong, *J. Pharm. Anal.*, 2024, 100952.

